INTECH
open science | open minds

OPEN ACCESS
ARTICLE

International Journal of Advanced Robotic Systems

Design and Analysis of a Bio-Inspired Wire-Driven Multi-Section Flexible Robot

Regular Paper

Zheng Li[1,*] and Ruxu Du[1]

1 Institute of Precision Engineering, Dept. Mechanical & Automation Engineering, The Chinese University of Hong Kong, Hong Kong
* Corresponding author E-mail: zli@mae.cuhk.edu.hk

Received 24 Jul 2012; Accepted 31 Jan 2013

DOI: 10.5772/56025

Abstract This paper presents a bio-inspired wire-driven multi-section flexible robot. It is inspired by the snake skeleton and octopus arm muscle arrangements. The robot consists of three sections and each section is made up of several identical vertebras, which are articulated by both spherical joints and a flexible backbone. Each section is driven by two groups of wires, controlling the bending motion in X and Y directions. This design integrates the serpentine robots' structure and the continuum robots' actuation. As a result, it is more compact than traditional serpentine robots and has a higher positioning accuracy than typical continuum soft robots, such as OctArm V. A Kinematics model and a workspace model of the robot are developed based on the piece wise constant curvature assumption. To evaluate the design, a prototype is built and experiments are carried out. The average distal end positioning error is less than 4%. Characteristics of the wire-driven robot are also discussed, including the leverage effect and the manipulability under constraint. These features makes the proposed robot well suited to confined spaces, especially for working in minimally invasive surgery, nuclear reactor pipelines, disaster debris, etc.

Keywords Bio-Inspired, Continuum Robot, Serpentine Robot, Wire-Driven Mechanism

1. Introduction

In the field of robotics, researchers have been building robots that mimic the appearance or function of their natural counterparts, such as serpentine robots and continuum robots. A Serpentine robot has a similar structure to the snake skeleton. It is composed of multiple links, with each link driven by a servomotor [1] or other actuators, e.g., pneumatic artificial muscles [2]. The idea of a continuum robot comes from the octopus' arm, elephant's trunk, mammal's tongue, etc. [3]. These two types of robot could be categorized as flexible robots. Compared with traditional discrete rigid robots, flexible robots are compliant, hence, well suited for confined environments. One typical example is the endoscope used in both medicine and industry. The medical endoscope helps surgeons performing minimally invasive surgery (MIS), e.g., the da Vinci surgical system [4]. In industry, endoscopes help to detect and repair damage to engineering devices, such as engines, pipelines and nuclear reactors [5]. It has become a common practice in industry. The flexible robot is also used for disaster relief after earthquakes, tsunamis, etc. [6].

The typical structure of a serpentine robot is a series of links, such as the ACM-Rx developed by S. Hirose [7], or

the OmniTread serpentine robot developed by J. Borenstein [8]. These links are articulated by the joint and each joint is actuated independently. For these serpentine robots, the links and joints are both rigid. The flexibility comes from the motion of the many joints. Current continuum robots have much fewer joints than serpentine robots. Their flexibility mainly comes from their soft structure, which could be driven by various power sources. For example, K. Suzumori, *et al*. developed a flexible micro actuator powered by compressed air [9], I. D. Walker and his team built the OctArm robot actuated by pneumatic artificial muscles [10], [11]. Since they are driven by compressed air, precision control is difficult. Also, the size of these robots is not suitable for surgical operations. P. Dupont and his team developed a meso-size continuum robot driven by pre-curved concentric tubes [12], [13]. The size of these robots is suitable for carrying out MIS and vivo experiments. However, it is difficult for them to follow an arbitrary trajectory. Moreover, as the concentric tubes bend on each other to position the end-effector, material fatigue is a concern. A similar work was done by R. J. Webster III and his team [14], [15]. R. H. Sturges proposed a design using tendons to control the flexible end of the endoscopy [16]. It has only one bending DOF. N. Simann and his team built a continuum robot with more DOFs driven by tendons [17], [18]. These tendons not only control the motion of the robot, but also serve as the backbone. Some useful features of this robot are investigated, such as force sensing [19]. The problem is the robot has difficulty bending at large angles, (e.g., 360°) due to the stiffness of the tendons. In industry, OC Robotics in UK built a "Snake Arm" for engineering inspections [20]. It is articulated by universal joints and driven by tendons. There are some other forms of actuation for continuum robots, such as shape memory alloy [21], and electro-active polymer [22]. However, few use the wire-driven mechanism.

This paper presents a bio-inspired wire-driven multi-section flexible robot. The structure is similar to traditional serpentine robots, i.e., a series of rigid links (called "nodes") serve as the vertebras. The vertebras are articulated by both spherical joints and a flexible backbone. The actuation of these robots is similar to that of continuum robots. The vertebras are grouped into three sections and each section is controlled by two pairs of wires for X and Y direction motions. It is able to expand its workspace by using the internal and/or external constraints.

The rest of the paper is organized as follows: Section II presents the design of the robot and the wire-driven mechanism. Section III presents the forward kinematics and inverse kinematics of the single-section robot. Section IV gives the kinematics of the multi-section robot. Section V shows the workspace model. Section VI presents the experiment results and discussion. Finally, Section VII contains the conclusions.

2. Robot Design and Wire-Driven Mechanism

2.1 Wire-Driven Robot Design

From an anatomical point of view, the snake body is composed of three major parts: the vertebral column, muscle and skin. The vertebral column consists of a series of similar bony vertebras extending from the occipital of the skull to the tip of the tail. Two successive bony vertebras together with the interposed intervertebral disc form a joint. These joints can deflect a small angle about the axis in all directions. Moreover, these joints together enable the snake to easily bend over 360 degrees, as shown in Figure 1(a) [27].

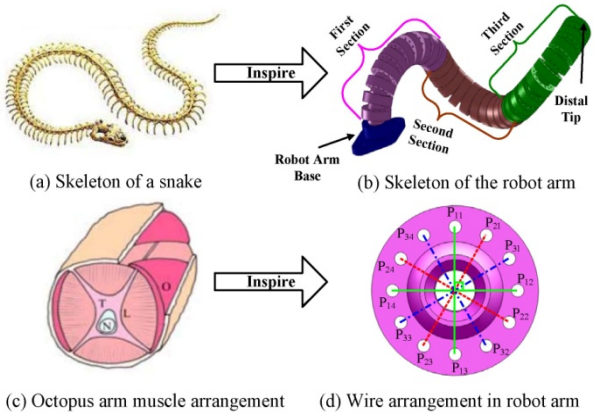

Figure 1. Wire-Driven Robot Arm Inspired by Snake Skeleton and Octopus Arm Muscle Arrangement

In our design, a number of "nodes" are used to imitate the bony vertebra of the snake, as shown in Figure 1(b). Two successive nodes form a spherical joint. Figure 2 shows the node and the spherical joint [24][25][26]. There are 12 pilot holes and a central cavity in each node. The outer diameter of the node is D = 20 mm, while the pilot holes are evenly distributed on a circle with a diameter of d = 15 mm. The height of each node is H = 6.5 mm, and the initial gap distance is h_0 = 2.5 mm. Detailed node design parameters are shown in table 1. The nodes have three functions: they are the skeleton of the robot; the pilot holes in the node guide the wires; and the central cavity of the node forms a channel, which could be used to deliver fluid or carry measuring instruments (such as optical fiber) and operating devices (such as knives and scissors) depending on the applications. Also, internal constraints can be deployed through the channel.

An octopus' arm is slender and highly flexible. It has three types of muscle as shown in Figure 1(c) [22]: longitudinal muscles (L), transversal muscles (T) and external oblique muscles (O). With these muscles, an octopus arm can easily extend, bend and twist. The longitudinal muscle, which is the major part, is

responsible for the bending function. In our design, we use four wires, which are divided into two groups, to imitate the longitudinal muscles for each section. As shown in Figure 2(a), P_{1x} (x = 1, 2, 3, 4, same as below) are for Section 1, P_{2x} are for Section 2, and P_{3x} are for Section 3. Each section has two bending DOFs. Take section one as an example, P_{11} and P_{13} control the upward and downward bending; while P_{12} and P_{14} control the leftward and rightward bending. These two groups of wires are orthogonally distributed and, as a result, the two bending motions are independent. Other sections are controlled in a similar manner. As shown in Figure 2(a), the pilot holes are evenly distributed, hence, the shift angle between each section is α = 30°. With this arrangement, the robot can bend in all directions. When two or more sections are involved, the robot can bend to "S" shapes or similar.

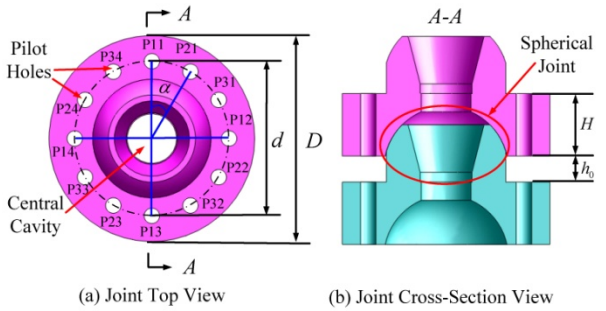

Figure 2. Joint of the Wire-Driven Robot

Figure 3 shows a cross-section view of the first section of the wire-driven flexible robot. The nodes are articulated by spherical joints and an elastic backbone. All the nodes are tightly connected to the backbone without being slippery. Wires go through the pilot holes and are fastened at the end of the section. When wire#2 contracts and wire#1 extends, the load acting on the robot is equivalent to an axial force and a moment. The axial strain is negligible because the nodes are rigid. As a result, the robot arm's motion is nearly pure bending. Without other external perturbations, the ideal deformation of the backbone is a circular arc as shown in the figure.

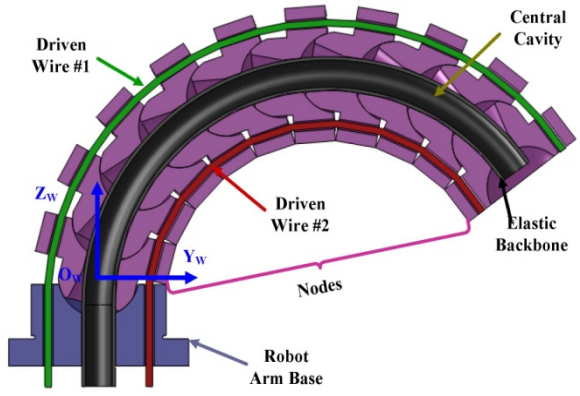

Figure 3. Cross-Section View of A Single Section

In practice, friction always exists. To minimize the side effects of friction, an elastic rubber tube is used to constrain the node bending. It serves as the flexible backbone of the robot. The elastic force of the backbone counteracts the disturbance of the friction. As a result, the nodes will bend evenly and the actual shape of the robot is a circular arc.

Outer Diameter (D)	20 mm
Inner Diameter (D1)	5 mm
Ball Diameter (D2)	12 mm
Reference Circle Diameter (d)	15 mm
Pilot Hole Diameter (d1)	1.5 mm
Number of pilot holes (N)	12
Node Height (H)	6 mm
Gap distance (h_0)	2.5 mm
Mass (M)	1.78g
Moment of Inertia Ixx	57.37 g·mm²
Moment of Inertia Izz	90.16 g·mm²

Table 1. Node Design Parameters

This design could easily be extended to multi-section robots. To build the multi-section robot, each section is connected sequentially as shown in Figure 1(b). Each section has two DOFs and is controlled by four wires. For general 3D motion, three sections would be sufficient.

2.2 Wire-Driven Mechanism

In the modelling of the wire-driven flexible robot, the joints are the fundamental element. The total bending angle of the robot depends on the number of joints and the joint bending angle θ. As mentioned previously, the bending of each joint is assumed to be identical. For each joint, the bending is illustrated in Figure 4. In the figure, the blocks represent the node, while the circle is the rotation centre. The parameters are as described previously.

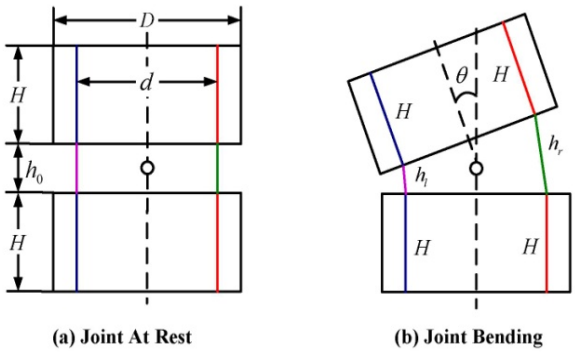

Figure 4. Illustration of the Joint Bending

The wire is divided into two parts: the part inside the robot arm and the part outside. Only the length change of the first part affects the robot's bending. Assume the robot has N nodes, at resting position the wire length inside the robot arm is as equation (1), where L_{l0} and L_{r0} are the initial length of left and right wire respectively.

$$L_{l0} = L_{r0} = L_0 = N \cdot (H + h_0) \quad (1)$$

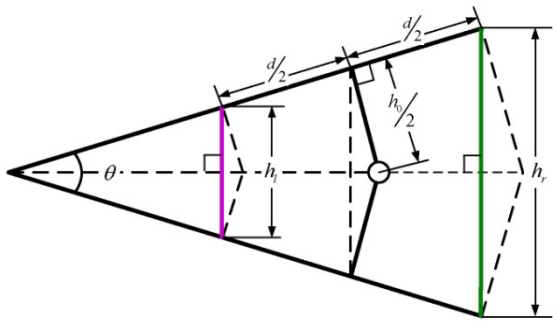

Figure 5. Wire Length Change due to Joint Bending

When each joint bends θ leftward, the gap distance changes and the wire length inside the node remains the same. For both wires, their length variation is as shown in Figure 5. For the left wire the gap distance decreases to h_l, while for the right wire it increases to h_r. Based on simple geometry, it can be shown that the gap distance after bending is as follows:

$$\begin{cases} h_r = h_0 + \left[d \cdot \sin\left(\frac{\theta}{2}\right) - 2h_0 \cdot \sin^2\left(\frac{\theta}{4}\right) \right] \\ h_l = h_0 - \left[d \cdot \sin\left(\frac{\theta}{2}\right) + 2h_0 \cdot \sin^2\left(\frac{\theta}{4}\right) \right] \end{cases} \quad (2)$$

In summation, the total wire length after bending is shown as below:

$$\begin{cases} L_r = L_0 + N\left[d \cdot \sin\left(\frac{\theta}{2}\right) - 2h_0 \cdot \sin^2\left(\frac{\theta}{4}\right) \right] \\ L_l = L_0 - N\left[d \cdot \sin\left(\frac{\theta}{2}\right) + 2h_0 \cdot \sin^2\left(\frac{\theta}{4}\right) \right] \end{cases} \quad (3)$$

From equation (3), the overall bending angle of the robot in terms of wire lengths is:

$$\Theta = N \cdot \theta = 2N \cdot \arcsin\left[\frac{L_r - L_l}{2N \cdot d} \right] \quad (4)$$

The maximum bending angle, θ_{max}, of the joint is constrained by the node parameters, D and h_0. The relationship between θ_{max} and the node parameters is as follows:

$$\theta_{max} = 2\arctan\left(\frac{h_0}{D}\right) \quad (5)$$

3. Kinematics of the Single Section Robot

The wire-driven flexible robot has multiple DOFs. However, the robot is underactuated. For each section, only two bending DOFs are controllable and are considered in the kinematics analysis. In this section, the kinematics of the single section robot is analyzed.

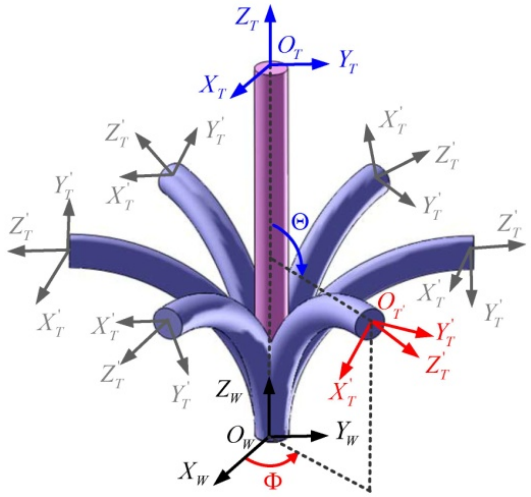

Figure 6. Single Section Bending Illustration

Figure 6 shows the bending of a single section wire-driven flexible robot. It could be described by the bending angle Θ and bending direction angle Φ. Θ is the central angle of the circular arc and Φ is the angle between the X axis and the bending plane. These two angles are determined by the length changes of the four wires. The distal end position and orientation can be determined when the two angles are known. Hence, the kinematics can be divided into two parts [3], [24] as shown in Figure 7. The first part is between the actuator space (i.e., wire length l) and the configuration space (i.e., bending angle Θ and direction angle Φ). In this part the forward and inverse kinematics are defined as f_1 and f_1^{-1} respectively. The second part is between the configuration space and the task space (i.e., distal end position (x, y, z) and orientation (n, o, a). The forward kinematics and inverse kinematics are defined as f_2 and f_2^{-1} respectively.

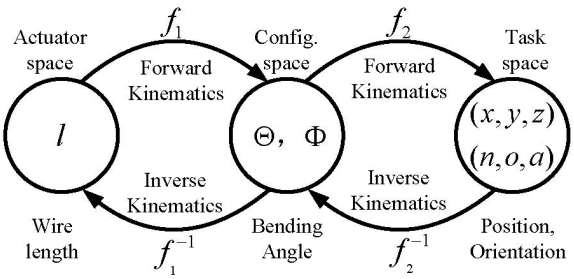

Figure 7. Kinematics Defined by Mapping between the Spaces

3.1 Mapping between the Actuator Space and the Configuration Space

Figure 8 shows the robot bending in an arbitrary direction. As shown in the figure, P_1 and P_3 control the bending about the Y axis, while P_2 and P_4 control the bending about the X axis. Their combination allows the robot to bend in an arbitrary direction (about the Y' axis). Otherwise, the bending plane is OX'Z.

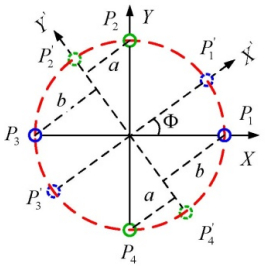

Figure 8. Robot Bending in an Arbitrary Direction

After bending, the wire length change is proportional to the distance between the wire and the neutral plane. For example, when the robot bends about the Y' axis, the bending direction angle is Φ. Although, the robot is flexed by the four wires P_1, P_2, P_3, P_4, it is equivalent to P_1'. P_3' controls the robot's bending while P_2' and P_4' lay in the neutral plane. The wire lengths of the four wires after bending are as follows:

$$P_1:\ L_1 = L_0 + 2N\left[b\cdot\sin\left(\frac{\theta}{2}\right) - h_0\cdot\sin^2\left(\frac{\theta}{4}\right)\right] \quad (6)$$

$$P_2:\ L_2 = L_0 + 2N\left[a\cdot\sin\left(\frac{\theta}{2}\right) - h_0\cdot\sin^2\left(\frac{\theta}{4}\right)\right] \quad (7)$$

$$P_3:\ L_3 = L_0 - 2N\left[b\cdot\sin\left(\frac{\theta}{2}\right) + h_0\cdot\sin^2\left(\frac{\theta}{4}\right)\right] \quad (8)$$

$$P_4:\ L_4 = L_0 - 2N\left[a\cdot\sin\left(\frac{\theta}{2}\right) + h_0\cdot\sin^2\left(\frac{\theta}{4}\right)\right] \quad (9)$$

where, $a = (d/2)\cdot\sin(\Phi)$ is the distance from P_2 and P_4 to the neutral axis Y' and $b = (d/2)\cdot\cos(\Phi)$ is the distance from P_1 and P_3 to Y'.

From the wire length, the robot's bending direction angle, i.e., Φ, and the robot's bending angle, i.e., Θ, can also be determined:

$$\Phi = \arctan\left(\frac{L_2 - L_4}{L_1 - L_3}\right) \quad (10)$$

$$\Theta = N\cdot\theta = 2N\cdot\arcsin\left[\frac{\sqrt{(L_1 - L_3)^2 + (L_2 - L_4)^2}}{2N\cdot d}\right] \quad (11)$$

Equations (6) ~ (9) define the inverse mapping between the actuator space and the configuration space, i.e., f_1^{-1}. The forward mapping, i.e., f_1, is given by Equations (10) and (11).

3.2 Mapping between the Configuration Space and the Task Space

The distal end position and orientation of the wire-driven flexible robot arm can be derived from the D-H method. However, a single section robot may have tens of nodes, which makes the process very complicated [24]. The alternative is to use geometric analysis. As the backbone lies in the neutral plane its length remains unchanged during the bending process. Also, the total length of the robot is constant and all the nodes have the same bending angle, which means the curvature of the backbone is constant within the section. The piece wise constant curvature assumption brings much convenience in deriving the kinematic model.

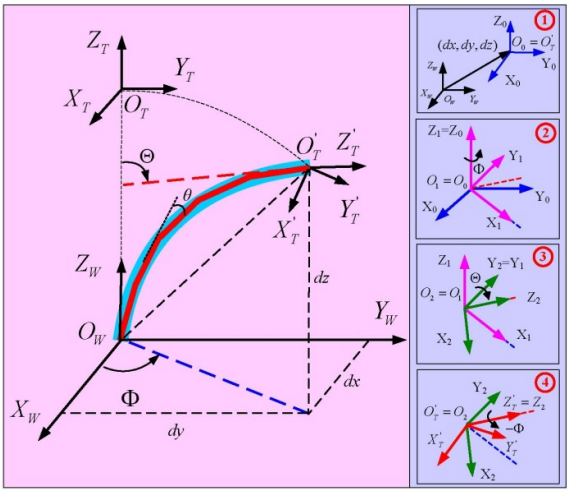

Figure 9. Single Section Robot Coordinate Transformation

Figure 9 illustrates the coordinate transformation of a single section robot. In the figure, the cyan thick solid curve represents the backbone, while the red poly line represents the node axis (as an example, five nodes are shown). Each node axis is a part of the regular polygon, whose exterior angle is θ and the side length is $H + h_0$. Based on geometry, the distal end position is found as:

$$\begin{cases} x = (H+h_0)\sum_{i=1}^{N}\sin\left[(i-1/2)\cdot\theta\right]\cos(\Phi) \\ y = (H+h_0)\sum_{i=1}^{N}\sin\left[(i-1/2)\cdot\theta\right]\sin(\Phi) \\ z = (H+h_0)\sum_{i=1}^{N}\cos\left[(i-1/2)\cdot\theta\right] \end{cases} \quad (12)$$

Note that,

$$\sum_{i=1}^{N}\sin\left[(i-1/2)\cdot\theta\right] = \frac{\sin^2(N\theta/2)}{\sin(\theta/2)} \quad (13)$$

$$\sum_{i=1}^{N}\cos\left[(i-1/2)\cdot\theta\right] = \frac{\sin(N\theta/2)\cos(N\theta/2)}{\sin(\theta/2)} \quad (14)$$

From the distal end position, it is not difficult to find the robot's bending angles:

$$\Theta = (N-1/2)\cdot\theta = \frac{2N-1}{N}\cdot\arctan\left(\frac{\sqrt{x^2+y^2}}{z}\right) \quad (15)$$

$$\Phi = \arctan\left(\frac{y}{x}\right) \tag{16}$$

In short, Equations (12) ~ (14) give the forward mapping between the configuration space and the task space, i.e., f_2, and Equations (15) and (16) give the inverse mapping, i.e., f_2^{-1}.

4. Kinematic of the Multi-Section Robot

4.1 Forward Kinematics

The kinematic model of the multi-section robot is developed based on the single section robot model. Each section is treated as a link, similar to links in a traditional robot arm. The difference is the links here have three DOFs, i.e., two bending DOFs and a translation DOF. For a traditional robot arm, the kinematics can easily be solved using the D-H method [28]. However, the traditional D-H method is not applicable here. Walker developed a modified D-H method for continuum robots [29]. The designed flexible robot has a serpentine structure and so this method cannot be applied directly. Here, the geometry method is still used.

Let us consider Figure 9 again, the world coordinate, $O_W = \{X_W, Y_W, Z_W\}$, is set at the centre of the first joint. The first joint is composed of the robot base and the first node. The robot distal end, $O_T = \{X_T, Y_T, Z_T\}$, is located at the end of the robot. When the robot section bends at an angle Θ and the angle between the X_W axis and the bending plane is Φ, the robot distal end is moved to $O'_T = \{X'_T, Y'_T, Z'_T\}$. As shown in the figure, the transformation from O'_T to O_W involves four steps: (1) translate the coordinate origin from O_W to O'_T; (2) rotate the coordinate frame about the new Z axis with angle Φ; (3) rotate about the new Y axis with angle Θ; and (4) rotate about the new Z axis with angle $-\Phi$. The overall transformation is described as:

$$^{W}T_T = \mathrm{Trans}(dx,dy,dz)\cdot \mathrm{Rot}(z,\Phi)\cdot \mathrm{Rot}(y,\Theta)\cdot \mathrm{Rot}(z,-\Phi) \tag{17}$$

where, d_x, d_y and d_z are the translational displacements in X_w, Y_w , and Z_w directions. They are also the distal end coordinates in the world coordinate frame O_w-$X_wY_wZ_w$, which are as shown in (12). As the node axis is the side of a regular polygon, the results can be simplified as (18) and (19). In the equations, R is the radius of the polygon's circum circle.

$$R = \frac{H + h_0}{2\sin(\theta/2)} \tag{18}$$

Therefore, the configuration of each section is defined by the bending parameters, i.e., Θ and Φ, and the robot structure parameters, i.e., node number N and node axis length ($H + h_0$).

$$\begin{cases} dx = R(1-\cos(\Theta))\cos(\Phi) \\ dy = R(1-\cos(\Theta))\sin(\Phi) \\ dz = R\sin(\Theta) \end{cases} \tag{19}$$

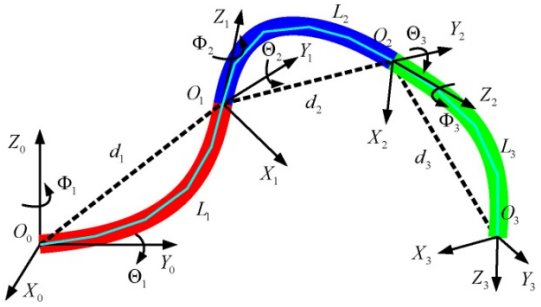

Figure 10. Multi-Section Robot Coordinate Transformation

As shown in Figure 10, once the transformation of each link is determined, the forward kinematics of a multi-section robot can be solved using the chain rule, which is the same as that of the D-H method [28]. Assume the robot has M sections, the distal end position and orientation in the world coordinate are:

$$^{W}T_M = {}^{W}T_1 \cdot {}^{1}T_2 \cdots {}^{M-2}T_{M-1} \cdot {}^{M-1}T_M \tag{20}$$

where $^{i-1}T_i$ is the transformation between section *i-1* and *i*, as shown in (21). In the equation, $C\Theta = \cos(\Theta)$, $S\Theta = \sin(\Theta)$, $C\Phi = \cos(\Phi)$ and $S\Phi = \sin(\Phi)$.

$$^{i-1}T_i = \begin{bmatrix} C\Theta C^2\Phi + S^2\Phi & (C\Theta-1)C\Phi S\Phi & S\Theta C\Phi & dx \\ (C\Theta-1)C\Phi S\Phi & C\Theta S^2\Phi + C^2\Phi & S\Theta S\Phi & dy \\ -S\Theta C\Phi & -S\Theta S\Phi & C\Theta & dz \\ 0 & 0 & 0 & 1 \end{bmatrix} \tag{21}$$

The overall transformation matrix is a 4 by 4 matrix. The first three columns give the orientation of the distal end, while the fourth column gives its position in the world coordinate system.

By now, the forward mapping from the configuration space to the task space has been established. For a multi-section robot, the mapping between the actuation space and the configuration space is basically the same as the single section robot. The difference is that the wire length change induced by former sections needs to be considered for later sections. The two sources of length change are superposed together. Note that, in determining the wire length for each section, the shift angle α shall be added to Φ for each section.

4.2 Inverse Kinematics

Similar to the traditional robot with many DOFs, the inverse kinematics of a multi-section flexible robot is complex. In most cases there is no unique solution as there is for single section robots. Walker, *et al*. proposed a closed-form inverse solution for multi-section continuum

robots [30]. In this method, besides the distal end position, the length of each section (i.e., d_1, d_2, d_3 in Figure 10) needs to be known. However, in general, these lengths cannot be predetermined. Since there are many ways to reach a desired position, we propose a method in which closed form inverse kinematics can be solved. It is called a uniform bending scheme.

In this scheme, the backbone radius for each section is the same, i.e., $R_1 = \ldots = R_M = R$. Also, all the bending motions are in the same plane, i.e., $\Phi_1 = \ldots = \Phi_M = \Phi$. In this design, each section has the same number of nodes. Hence, we have $\Theta_1 = \ldots = \Theta_M = \Theta$. From equations (18) - (21), the multi-section robot forward kinematics in this scheme becomes:

$$\begin{bmatrix} x \\ y \\ z \end{bmatrix} = \sum_{j=1}^{M} \begin{bmatrix} R \cdot \sin\left[(j-1/2)\cdot\Theta\right]\cdot\left[1-\cos(\Theta)\right]\cdot\cos(\Phi) \\ R \cdot \sin\left[(j-1/2)\cdot\Theta\right]\cdot\left[1-\cos(\Theta)\right]\cdot\sin(\Phi) \\ R \cdot \cos\left[(j-1/2)\cdot\Theta\right]\cdot\sin(\Theta) \end{bmatrix} \quad (22)$$

By solving this equation, it follows that:

$$\Phi = \arctan(\frac{y}{x}) \quad (23)$$

$$R = \frac{x^2 + y^2 + z^2}{2\sqrt{x^2 + y^2}} \quad (24)$$

$$\Theta = \frac{1}{M}\arcsin\left(\frac{z}{R}\right) \quad (25)$$

After the configurations of each section are determined, the wire lengths can be solved as in the previous section. It is interesting to note that, since each section has the same length and bending angle Θ, they can be treated as a node with variable length as in the single section case. Hence, the multi-section inverse kinematic problem becomes the single section case. Although this simple case is one of many, it is useful in robot manipulation.

5. Workspace

The workspace of the wire-driven flexible robot is derived from the forward kinematics. The workspace is determined by the robot's structure, i.e., the maximum joint rotation angle and vertebra number in each section. For a single section robot, the workspace is simple. It could be expressed as follows:

$$\sqrt{x^2 + y^2 + z^2} = (H + h_0)\frac{\sin(N \cdot \theta/2)}{\sin(\theta/2)} \quad (26)$$

From Equation (26), it can be seen that the workspace is a spheroidal surface. In planes parallel to the XY plane, the locus of the robot distal end is a circle, whose radius depends on the joint bending angle and the parameters of the node. Note that the workspace is circularly symmetric and can be found by rotating the distal end trajectory in the X-Z plane about the Z axis.

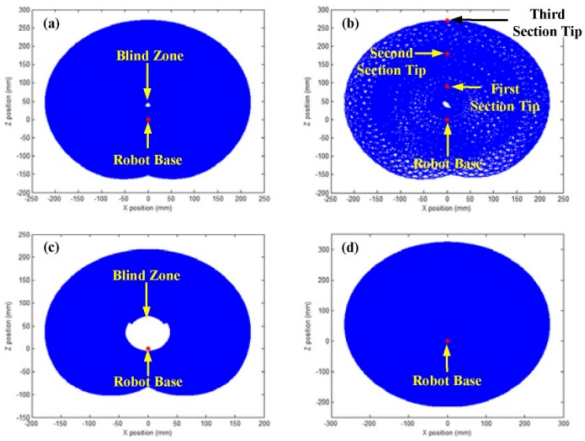

Figure 11. The Workspace in A X-Z Plane of A 3-Section Robot. (a) N=10, simulation interval is 2.5° ; (b) N=10, simulation interval is 10 °; (c) N=8, simulation interval is 2.5° ; (d) N=12, simulation interval is 2.5° .

The workspace for a multi-section robot is rather complex. It is not a surface but a 3D space. In general, there is no analytical solution but it can be solved numerically. Figure 11(a) shows the workspace of the three section robot when the bending is confined to the XZ plane. The bending interval, $\Delta\Theta$, used for the simulation is 2.5º. The blue curves indicate the reachable positions of the distal end while the red dot is the robot base. The workspace is symmetric. Figure 11(b) shows the same workspace when the simulation interval is increased to 10º. It is noted that, the trajectory distribution of the robot distal end is not even. The denser the curves, the more configurations the robot can reach at the same position, or, in other words, the more dexterous the robot is. From the simulation, it is shown that the robot is more dexterous near the second section. It is also noted that, there is a blind zone, which the robot distal end cannot reach, inside the workspace. The existence and size of the blind zone is determined by the robot arm's structure, i.e., the maximum bending angle of each section. When there are 8 vertebras in each section, the blind zone is shown in Figure 11(c). When the number of vertebra in each section increases to 12, the blind zone vanishes, as shown in Figure 11(d). One necessary condition for illuminating the blind zone is whether the robot arm can reach its base, or if the maximum bending angle of the whole robot arm is 360°.

6. Experiment and Discussions

To validate the design, a prototype was built as shown in Figure 12. The robot has three sections. Each section has 10 nodes, which are made by Rapid Prototyping (RP). The dimensions of the nodes are as shown in Section II. In this design, the maximum bending angle for each joint is

14.25°. A 5 mm diameter rubber tube is used as the flexible backbone. Six groups of steel wires with 0.475 mm diameter are used to control the robot. These wires are pulled by servomotors, whose maximum torque is 13 kg·cm. The controller is developed using the commercial micro control unit ATmega 128 [31].

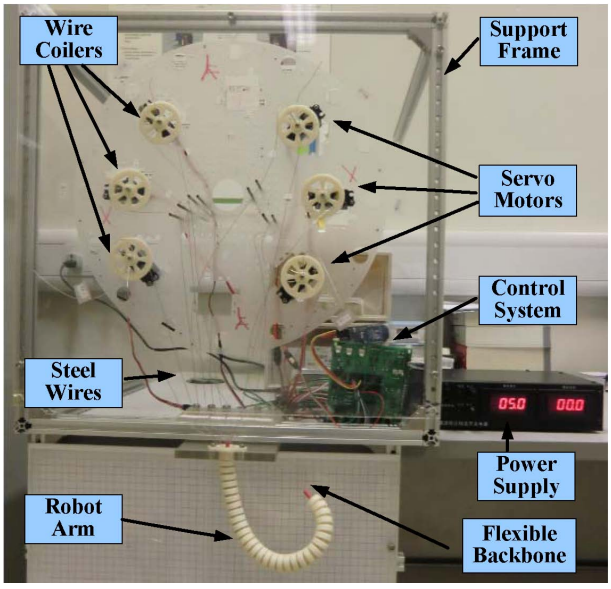

Figure 12. Experiment Setup of Wire-Driven Serpentine Robot

6.1 Positioning Accuracy Study

The bending shapes of the robot could be various. Figure 13(a) shows the robot at its resting position and Figures (b) ~ (l) show various bending cases.

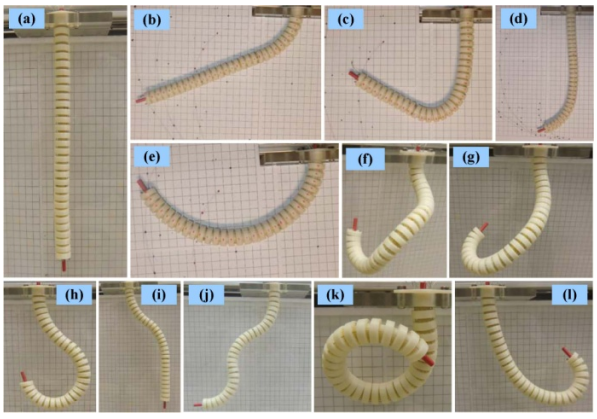

Figure 13. Different Bending Cases

In particularly, four cases, namely, (b), (c), (d) and (e) are studied in detail. In these cases, the three sections all bend in the X-Z plane. The bending angles for each section are shown in Table 2. In the case of (b), only the section near the robot base bends. The other two sections remain still. In the case of (c) and (d), only the second and third sections bend, respectively. In the case of (e), the three sections bend together and their bending angles are the same. In the test, no payload is applied to the robot. The power of the robot is affected by the motion type and robot configuration. Generally, the power consumption of each motor is less than 1W and the power consumption of the control system is around 0.5W. At larger bending angles, a bigger moment is needed to maintain the configuration of the robot. The more motors involved in the motion and the larger the bending angle, the higher the power consumption of the robot.

	Section 1	Section 2	Section 3
Case (b)	0 ~ 142.5°	0	0
Case (c)	0	0 ~ 142.5°	0
Case (d)	0	0	0 ~ 142.5°
Case (e)	0 ~ 142.5°	0 ~ 142.5°	0 ~ 142.5°

Table 2. The Bending Angles in the Experiment

In the four cases, the trajectories of the distal end are measured using a grid paper, as shown in Figure 12. They are compared with the model predictions. The results are shown in Figure 14. The curves are the predicted distal end trajectory, while the dots are the recorded ones. Case (b) is shown in red; Case (c) is in green; Case (d) is in blue and Case (e) is in magenta. The experiment results and the model predictions match reasonably well.

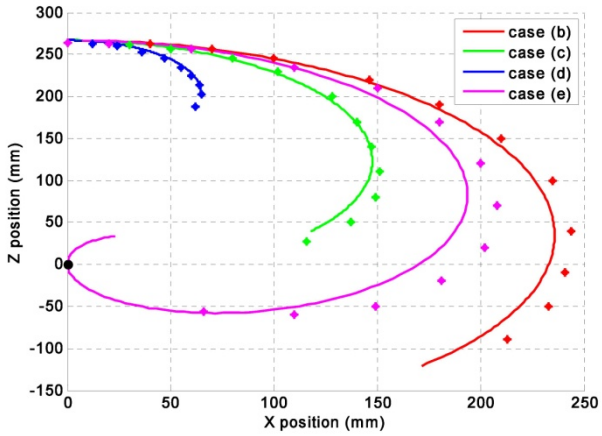

Figure 14. Trajectories of The Distal End

Figure 15 shows the relative positioning error. The curves show the error in each measured position, while the dashed lines show the average error. From the figure, it is seen that the average positioning error in the four cases is 2.372%, 1.627%, 0.871% and 3.581% respectively. These results are consistent with the results reported in [24]. It should be pointed out that the positioning error is smaller than that of the continuum robot. As reported in [30], the average prediction error of OctArm V using a piecewise constant curvature model is nearly 50% of the robot length. A close examination reveals that the longer the moving part, the larger the error. The reason would be: on the one hand the flexibility of the robot increases with the growing of the moving part length; on the other hand, the error near the robot base is accumulated and would be amplified at the distal end.

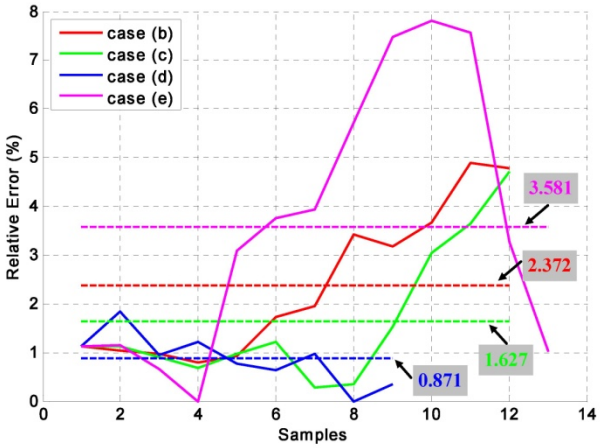

Figure 15. Relative Positioning Error of the Distal End

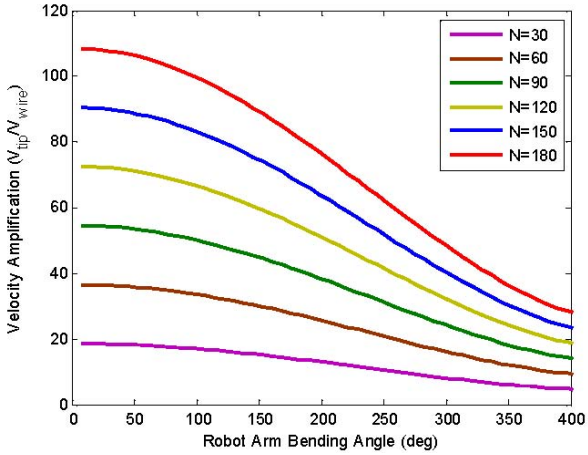

Figure 16. Velocity Amplification of Wire Driven Flexible Robot

Compared with the traditional rigid discrete robot, the positioning accuracy of the wire-driven robot is low. Also, it is more affected by the robot's configuration and external perturbations. As a result, such a robot is more suitable for inspection applications, e.g., endoscopy. To improve the accuracy one could use a position feedback control similar to the approaches used in continuum robots [33].

6.2 Robot Characteristic Study

A. Leverage Effect

From the previous section, it can be seen that the positioning error of the wire-driven robot could be amplified at the distal end. This is due to the amplification of the displacement from the base to the distal end. Because of this amplification, the velocity would also be amplified.

Figure 16 shows the ratio of the distal end velocity to the wire velocity for a single section robot with different numbers of nodes. From the figure, it can be seen that with a large number of nodes (i.e., when the robot is long), the velocity can be amplified over 100 times. This could explain why the pike can generate an acceleration of over 25g [32]. Even if the muscle contraction is small, the pike could from a C shape and release quickly. The leverage effect is important in teleoperation as it will reduce the resolution of the robot. Theoretically, when there is no payload, the positioning resolution of the end effector is the actuator resolution multiplied by the leverage ratio. The larger the ratio is, the lower the positioning resolution. In this prototype, the resolution of the servo motor is 0.09° and the lowest positioning resolution of the end effector is 0.47mm, which is at its resting position. It is noted that the ratio is not a constant. It depends on the robot's bending angle. The initial ratio is the robot length over the wire distance. As the bending angle increases, the ratio decreases.

B. Controllability under constraint

Another distinct feature of the wire-driven flexible robot is its controllability under constraint, i.e., when some of the nodes are fixed, the robot is still controllable. For continuum robots, researchers usually consider how to avoid obstacles and perform path planning [14]. However, we can actually employ these obstacles to change the shape of the robot and control the distal end reach positions in situations where they were unreachable beforehand [24]. Take the single section robot as an example.

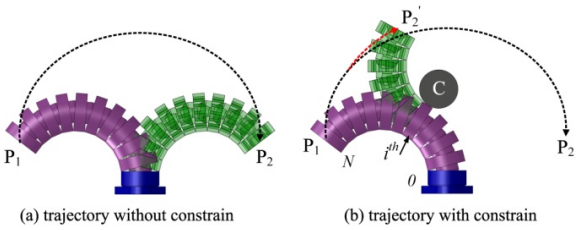

Figure 17. Distal End Trajectory Affected by External Constraint

Figure 17(a) shows the robot distal end trajectory without external constraints. The robot bends from P_1 to P_2. When there is a constraint C, as shown in Figure 17(b), the bending of the robot is changed. It bends from P_1 to P_2'. This implies that with constraints the robot would reach different positions. The altered trajectory is predictable when the position of the constraint is known. The kinematics model under constraints could be derived following the procedures below:

- Step 1: recall the unconstrained kinematics model;
- Step 2: find the number (i) of the node being constrained;
- Step 3: get the position and orientation of the i^{th} node;
- Step 4: take the i^{th} node as the new robot base and apply the kinematics model, where the node number $N'=N-i$;
- Step 5: add the two parts together, and get the position and orientation of the distal end.

Figure 18 shows an example of the predicted robot distal end trajectory with constraint. In the figure, the dash curves are the robot distal end trajectories, the poly lines are the node axis, the circles denote the joints, and the square is the constraint. It should be mentioned that there are a few ways to find the constrained node, such as stereo vision [33], or magnetic sensor [34]. This feature is helpful in applications such as nuclear reactor inspections, disaster relief, etc.

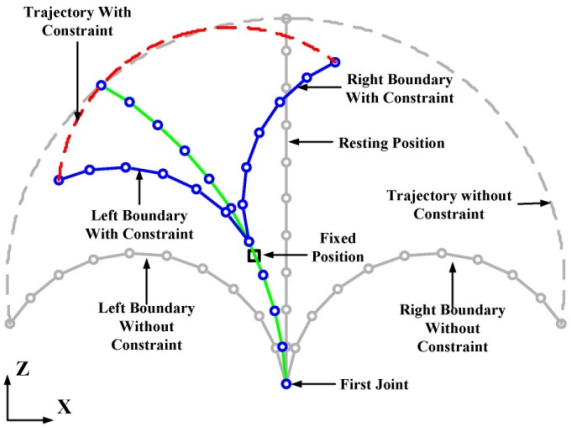

Figure 18. Example of Robot Trajectory under Constraint

7. Conclusions

This paper presents the design and analysis of a bio-inspired wire-driven multi-section flexible robot. Based on the discussions above, the following conclusions can be made:

1. The wire-driven flexible robot is a combination of the serpentine robot and the continuum robot. The structure is snake like, while the actuation is similar to that of the continuum robot. With this design, the robot is simpler than traditional serpentine robots and has higher positioning accuracy than typical continuum robots.
2. The kinematics of the wire-driven flexible robot is derived in a way similar to that used in continuum robots. For multi-section robots, each section is treated as a link with 3DOFs. Closed form inverse kinematics is found for multi-section robots working in a uniform bending scheme. The workspace of a single section robot is a spheroidal surface. For multi-section robots, there could be a blind zone inside the workspace depending on the maximum section bending angle.
3. A leverage effect is found for the wire-driven mechanism. The position, velocity, and acceleration of the robot's distal end could be much higher than that of the actuator. The ratio depends on the robot's length as well as the distance between the wire pair. For any given design, the ratio is not constant. It varies with the robot configuration. The maximum ratio is at its resting position.
4. The wire-driven flexible robot remains controllable under internal or external constraints. The kinematics model could be easily derived following the suggested method. The robot could reach new positions that are unreachable without the constraint, as a result, expanding its workspace.

8. References

[1] J. K. Hopkins, B. W. Spranklin and S. K. Gupta, "A survey of snake-inspired robot designs", *Bioinspiration & Biomimetics*, Vol. 4, pp. 1-19, 2009.

[2] J. Borenstein, M. Hansen and A. Borrell, "The OmniTread OT-4 Serpentine Robot - Design and Performance", *Journal of Field Robotics*, Vol. 24, pp. 601-621, 2007.

[3] R. J. Webster and B. A. Jones, "Design and Kinematic Modeling of Constant Continuum Robots: A Review," *Int. J. of Robotics Research*, Vol. 29, pp. 1661-1683, 2010.

[4] "The Da Vinci surgical system" at: http://www.intuitivesurgical.com/products/davinci_surgical_system/

[5] V. V. Klyuev and Y. K. Fedosenko, "50TH Anniversary of Non-Destructive Testing In Russia", 17th World Conference on Non-Destructive Testing, 25-28, Oct. 2008, Shanghai, China, pp. 1-9, Oct. 2008.

[6] A. Hirayama and K. Ito, "Development of rescue manipulator to search narrow space for victims," *Artificial Life Robotics*, Vol. 13, pp. 331-335, 2008.

[7] S. Hirose and M. Mori, "Biologically Inspired Snake-like Robots", Proceedings of the 2004 IEEE International Conference on Robotics and Biomimetics, Aug. 22-26, 2004, Shenyang, China, Aug. 2004.

[8] G. Granosik, M. G. Hansen and J. Borenstein, "The OmniTread Serpentine Robot for Industrial Inspection and Surveillance", *International Journal on Industrial Robots*, Special Issue on Mobile Robots, Vol. IR32-2, pp. 139-148, 2005.

[9] K. Suzumori, S. Iikura and H. Tanaka, "Development of Flexible Microactuator and Its Applications to Robotic Mechanisms", *Proceedings of the 1991 IEEE International Conference on Robotics and Automation*, Sacramento, Califonia, pp. 1622-1627, 1991.

[10] M. D. Grissom, I.D. Walker *et al.*, "Design and experimental testing of the OctArm soft robot manipulator", Proc. of SPIE, 2006. At: http://dx.doi.org/10.1117/12.665321.

[11] W. McMahan, I.D. Walker *et al.*, " Field Trials and Testing of the OctArm Continuum Manipulators", *Proceedings of 2006 IEEE International Conference on Robotics and Automation*, Orlando, Florida, pp. 2336-2341, 2006.

[12] P. E. Dupont, J. Lock, B. Itkowitz and E. Butler, "Design and Control of Concentric-Tube Robots," *IEEE Trans. Robotics*. Vol. 26, No. 2, pp. 209-225, 2010.

[13] P. Sears and P. E. Dupont, "Inverse Kinematics of Concentric Tube Steerable Needles", *2007 IEEE International Conference on Robotics and Automation*, Roma, Italy, pp.1887-1892, April 2007.
[14] L. A. Lyons, R. J. Webster III and R. Alterovitz, "Motion Planning for Active Cannulas", IEEE/RSJ International Conference on Intelligent Robots and Systems (IROS), pp. 801-806, Oct. 2009.
[15] D. C. Rucker, B. A. Jones, and R. J. Webster III, "A Geometrically Exact Model for Externally Loaded Concentric-Tube Continuum Robots", IEEE Transactions on Robotics, Vol. 26, No.5, Oct. 2010.
[16] R. H. Sturges, S. Laowattana *et al*., "A flexible tendon-controlled device for endoscopy", *Proceedings of the 1991 IEEE International Conference on Robotics and Automation*, Sacramento, California, April, 1991, pp. 2582-2591, Apr. 1991.
[17] N. Simaan, K. Xu, W. Wei, A. Kapoor, P. Kazanzides, R. Taylar and P. Flint, "Design and Integration of a Telerobotic System for Minimally Invasive Surgery of the Throat", *The International Journal of Robotics Research*, 28 (9), pp. 1134-1153, 2009.
[18] K. Xu and N. Simaan, "Analytic Formulation for Kinematics, Statics, and Shape Restoration of Multibackbone Continuum Robots Via Elliptic Integrals," *J. of Mechanisms and Robotics*, Vol. 2, doi: 011006-1, Feb. 2010.
[19] K. Xu and N. Simaan, "An Investigation of the Intrinsic Force Sensing Capabilities of Continuum Robots", *IEEE Transactions on Robotics*, Vol. 24, No. 3, pp. 576-587, Jun. 2008,.
[20] "Snake Arm Robot," at: http://www.ocrobotics.com/
[21] T. Mineat, *et al*., "An active guide wire with shape memory alloy bending actuator fabricated by room temperature process", Sensors and Actuators, Vol. 97-98, pp. 632-637, 2002.
[22] C. Laschi, B. Mazzolai, el. "Design of a biomimetic robotic octopus am", *Bioinspiration & Biomimetics*, vol. 4, 2009 015006.
[23] "Modular Snake Robots," at: http://www.cs.cmu.edu/~biorobotics/
[24] Z. Li, R. Du, M. C. Lei, S. M. Yuan, "Design and Analysis of a Biomimetic Wire-Driven Robot Arm," *Proceedings of the ASME 2011 International Mechanical Engineering Congress & Exposition*, November 11-17, 2011, Denver, Colorado, USA.
[25] M. C. Lei and R. Du, "A Study on the Bending Mechanism of the Flexible Ureteroscope", *Proceedings of International Conference on Control and Automation Systems (ICCAS) 2010*, October 27-30, Gyeonggi-do, Korea.
[26] M. C. Lei, and R. Du, "Geometry Modeling and Simulation of the Wire-Driven Bending Section of a Flexible Ureteroscope," *Proceedings of World Congress on Engineering and Computer Science (WCECS) 2011*, October 19-21, 2011, San Francisco, California, USA.
[27] D. Drew, "Skeleton," at: http://k-8visual.info/ia_skeleton.html
[28] R. Hartenberg and J. Denavit, "Kinematic Synthesis of Linkages", New York: McGraw-Hill, 1964.
[29] B. A. Jones and I. D. Walker, "Kinematics for Multisection Continuum Robots," *IEEE Trans. on Robotics*, vol. 22, No.1, pp.43-57, Feb. 2006.
[30] S. Neppalli, M. A. Csencsits, B. A. Jones, I. D. Walker. "Closed-Form Inverse Kinematics for Continuum Manipulators", *Advanced Robotics*, Vol. 23, pp.2077-2091, 2009.
[31] "ATmega128 Micro Control Unit" at: http://atmel.com/dyn/products/product_card.asp?part_id=2018
[32] D. G. Harper, R. W. Blake, "Fast-start performance of rainbow trout Salmo gairneri and northern pike Esoxlucius". *Journal of Experimental Biology*, Vol. 150, 1990, pp.321-342.
[33] J. M. Croom, D. C. Rucker, J. M. Romano and R. J. Webster III, "Visual Sensing of Continuum Robot Shape Using Self-Organizing Maps", 2010 IEEE International Conference on Robotics and Automation, Anchorage, Alaska, USA, pp. 4591-4596.
[34] A. Bajo and N. Simaan, "Finding Lost Wrenches: Using Continuum Robots for Contact Detection and Estimation of Contact Location", *2010 IEEE International Conference on Robotics and Automation*, Anchorage, Alaska, May, 2010, pp. 3666-3673.